

Geophysical Research Letters

RESEARCH LETTER

10.1029/2019GL084354

Special Section:

Studies of the 2018/Mars Year
34 Planet-Encircling Dust
Storm

Key Points:

- Transport of water vapor is simulated during the 2018 global dust storm on Mars in the GEM-Mars General Circulation Model
- The simulation explains NOMAD observations of enhanced high-altitude water abundances during the global dust storm
- The vertical distribution of dust is a key factor for the transport of water vapor through the equatorial hygropause

Correspondence to:

L. Neary,
lori.neary@aeronomie.be

Citation:

Neary, L., Daerden, F., Aoki, S., Whiteway, J., Clancy, R. T., Smith, M., et al. (2020). Explanation for the increase in high-altitude water on Mars observed by NOMAD during the 2018 global dust storm. *Geophysical Research Letters*, 47, e2019GL084354. <https://doi.org/10.1029/2019GL084354>

Received 8 JUL 2019

Accepted 29 AUG 2019

Accepted article online 3 SEP 2019

Explanation for the Increase in High-Altitude Water on Mars Observed by NOMAD During the 2018 Global Dust Storm

L. Neary¹ , F. Daerden¹ , S. Aoki¹ , J. Whiteway² , R. T. Clancy³ , M. Smith⁴ , S. Viscardi¹ , J.T. Erwin¹ , I. R. Thomas¹ , G. Villanueva⁴ , G. Liuzzi⁴ , M. Crismani⁵ , M. Wolff³ , S. R. Lewis⁶ , J. A. Holmes⁶ , M. R. Patel⁶ , M. Giuranna⁷ , C. Depiesse¹ , A. Piccialli¹ , S. Robert¹ , L. Trompet¹ , Y. Willame¹ , B. Ristic¹ , and A. C. Vandaele¹ 

¹Royal Belgian Institute for Space Aeronomy, Brussels, Belgium, ²Centre for Research in Earth and Space Science, York University, Toronto, Ontario, Canada, ³Space Science Institute, Boulder, CO, USA, ⁴NASA Goddard Space Flight Center, Greenbelt, MD, USA, ⁵NPP/USRA, NASA Goddard Space Flight Center, Planetary Systems Laboratory, Greenbelt, MD, USA, ⁶School of Physical Sciences, The Open University, Milton Keynes, UK, ⁷Istituto di Astrofisica e Planetologia Spaziali, Istituto Nazionale di Astrofisica, Rome, Italy

Abstract The Nadir and Occultation for Mars Discovery (NOMAD) instrument on board ExoMars Trace Gas Orbiter measured a large increase in water vapor at altitudes in the range of 40–100 km during the 2018 global dust storm on Mars. Using a three-dimensional general circulation model, we examine the mechanism responsible for the enhancement of water vapor in the upper atmosphere. Experiments with different prescribed vertical profiles of dust show that when more dust is present higher in the atmosphere, the temperature increases, and the amount of water ascending over the tropics is not limited by saturation until reaching heights of 70–100 km. The warmer temperatures allow more water to ascend to the mesosphere. Photochemical simulations show a strong increase in high-altitude atomic hydrogen following the high-altitude water vapor increase by a few days.

Plain Language Summary The ExoMars Trace Gas Orbiter (TGO) is currently in orbit around Mars measuring the composition of the atmosphere. TGO was able to make observations before, during, and after a large planet-encircling dust storm that occurred from June to August 2018. The TGO measurements provide the first opportunity to observe how water vapor is distributed with height in the atmosphere during a global-scale dust event. It was found that there was a large increase in water vapor very high (40–100 km) in the atmosphere during the dust storm. Using a three-dimensional numerical model of the Mars atmosphere, we found that when dust from the storm is transported up to levels above ~40 km, it warms the atmosphere due to solar absorption, and this in turn prevents ice clouds from forming at heights of 40–60 km and allows more water vapor to ascend to greater heights in the atmosphere. This is of interest in terms of the planetary evolution, as water molecules at greater heights are more readily dissociated by sunlight and lost from the atmosphere. This is an important factor for understanding the changes that have occurred since the period when surface features on Mars indicate that liquid water was present.

1. Introduction

The planet-encircling global dust storm (GDS) on Mars in 2018 provided the first opportunity since 2007 to study the effects of such an event on the distribution of trace gases in the atmosphere. The ExoMars Trace Gas Orbiter (TGO), in orbit around Mars during the storm, carries two instruments designed to measure the composition of the atmosphere with unsurpassed spectral and vertical resolution: the Nadir and Occultation for Mars Discovery (NOMAD; Vandaele et al., 2018) and the Atmospheric Chemistry Suite (ACS; Korabiev et al., 2018, 2019). These instruments began science operations in April 2018, well before the GDS started, and monitored its full evolution from onset to decay from June to August 2018. The NOMAD water vapor retrievals during the GDS have been reported elsewhere (Vandaele et al., 2018; Aoki et al., 2019). This study has applied numerical simulations of the atmosphere of Mars to determine the processes that caused the increase in water vapor during the GDS of 2018.

During the 2007 GDS, observations from the Mars Express Spectroscopy for Investigation of Characteristics of the Atmosphere of Mars infrared (IR) spectrometer observed an increase of water vapor at high latitudes

(Fedorova et al., 2018). A similar result was inferred from Mars Climate Sounder (MCS) temperature and ice optical depth profiles (Heavens et al., 2018). The TGO NOMAD and ACS instruments also measured an increase in water vapor at high altitude during the GDS in 2018, which occurred much earlier than the 2007 GDS and also was much stronger (Vandaele et al., 2019; Aoki et al., 2019). The enhancement of high-altitude water vapor has been linked to reinforced hydrogen escape (Chaffin et al., 2017, 2019; Heavens et al., 2018; Krasnopolsky, 2019).

The present paper will report on numerical simulations in a 3-D Mars general circulation model (GCM) that were carried out to determine the processes that caused the high-altitude water vapor abundances observed during the 2018 GDS. During a GDS, the enhanced atmospheric dust content will lead to an increase of the atmospheric temperatures due to absorption of solar and IR radiation. This causes an expansion of the atmosphere and reinforces the global circulation's Hadley cells, which in turn transport dust and trace gases up to the lower mesosphere (40–60 km; Vandaele et al., 2019; Shaposhnikov et al., 2019; Clancy et al., 2010; Clancy et al., 2019). However, at the middle and upper mesospheric altitudes (60–100 km) where a strong increase of water vapor is observed during the GDS, there is no similar strong increase in atmospheric dust content observed (Fedorova et al., 2018; Vandaele et al., 2019). The mechanisms that cause the strong increase in water vapor at those altitudes must therefore be only indirectly related to dust and the reinforced global circulation.

The transition region between high and low water vapor abundances is controlled by saturation conditions and is usually referred to as a “hygropause.” Under normal conditions on Mars, the hygropause occurs at altitudes of 20–50 km (depending on season) over low latitudes. Poleward from midlatitudes, the height of the hygropause decreases (Daerden et al., 2019, their Figure 13). In a similar fashion, in the atmosphere of the Earth, the temperature minimum at the tropopause forms a barrier for water vapor transport from the troposphere into the stratosphere (Holton & Gettelman, 2001). In GDS conditions with increased temperatures, it can be expected that the hygropause would occur at greater heights (Heavens et al., 2018); however, this mechanism was never explicitly simulated in Mars GCMs. Shaposhnikov et al. (2019) presented a simulation of water vapor transport in the 2007 GDS. High-altitude water was explained by a strengthening of the southern hemispheric Hadley circulation cell, which is particularly strong near southern summer solstice (when the 2007 GDS occurred). Here we present the first simulations for the 2018 GDS, which occurred near equinox, with model comparisons to direct retrievals of new and unique high vertical resolution water vapor vertical profiles from the NOMAD instrument (Aoki et al., 2019). As our GCM contains an interactive calculation of atmospheric gas and photochemistry processes (Daerden et al., 2019), we also address the impact on the dissociation of water and escape from the atmosphere.

2. Model and Scenario Description

The GEM-Mars model is described and evaluated in Neary and Daerden (2018) and Daerden et al. (2019). The model uses a grid point dynamical core with staggered log-pressure vertical levels simulating the atmosphere up to ~150 km. The simulations for this work were performed with a horizontal resolution of $4^\circ \times 4^\circ$ and a dynamical time step of 1/48th of a Mars day (sol). The model includes a wide set of physical parameterizations for the Mars atmosphere. This includes radiative transfer through dust, CO₂, and water ice clouds, heat transfer through the soil, interactive CO₂, pressure, dust and water cycles, size distributed dust particles, and a simple cloud formation scheme with a mono disperse water ice particle distribution. Surface and planetary boundary layer turbulent mixing, molecular diffusion, and gravity wave drag are parameterized (Neary & Daerden, 2018), and gas and photochemistry are included (Daerden et al., 2019; Encrenaz et al., 2019; Smith et al., 2018). The radiative transfer code includes a two-stream method (Toon et al., 1989) applied in five wavelength bands in the visible and IR range. For dust, the optical properties are the same as in Madeleine et al. (2011), Table 2, Case 2. For water ice, the optical properties are calculated using Bohren-Huffman Mie scattering code (original program taken from Bohren & Huffman, 1983, Appendix A, modified by B.T. Draine, Princeton Univ. Obs. 26/10/1990) with refractive indices from Warren and Brandt (2008).

The GEM-Mars model includes the option to simulate a generic Mars year with a dust distribution computed using a scheme to lift dust from the surface by saltation (Daerden et al., 2015; Musiolik et al., 2018; Neary & Daerden, 2018). To study a specific year, the dust total column optical depth can be scaled to a climatological scenario (Montabone et al., 2015), while maintaining the same vertical profile shape. In previous versions of

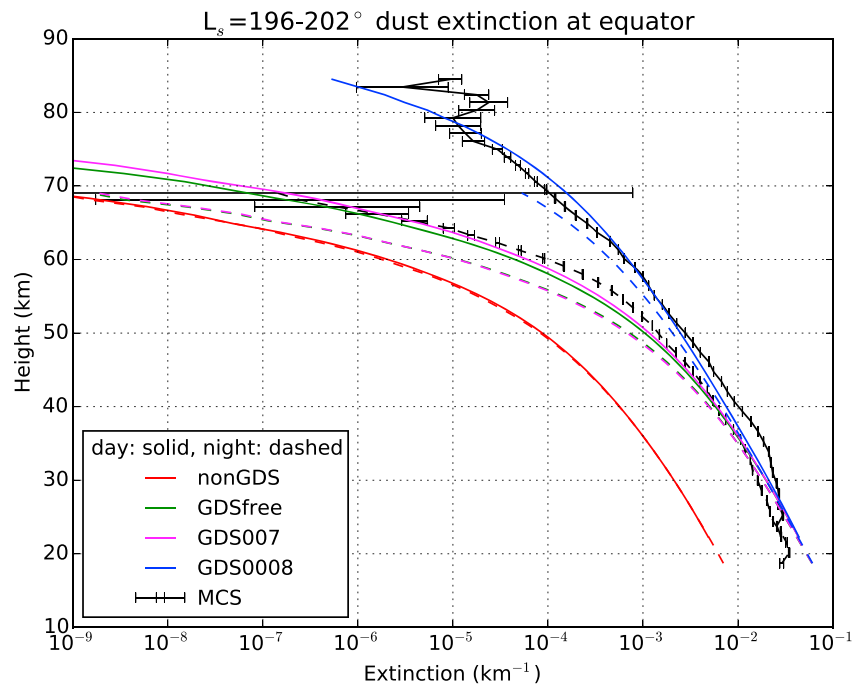


Figure 1. Average profiles of dust optical extinction coefficient at wavelength $0.67 \mu\text{m}$ at the equator for the period of L_s 196–202°. The black lines are Mars Climate Sounder (MCS) data, red is the simulated dust profile from the dust lifting scheme with no scaling, green is the same free dust profile with the column scaled to MY34, magenta is the dust profile prescribed with Conrath parameter of $\nu = 0.007$ and scaled to MY34, and blue is Conrath parameter of $\nu = 0.0008$ and scaled to MY34. Both day (solid) and night (dashed) profiles are shown for all data. GDS = global dust storm.

GEM-Mars, we averaged the daily maps from the climatology every $10^\circ L_s$ (Giuranna et al., 2019; Neary & Daerden, 2018), but to capture the rapid onset of the 2018 storm, we update the maps daily. The new 2018–2019 maps are described in Montabone et al. (2020). They were generated using data from the MCS (Kleinböhl et al., 2009, 2011) on the NASA Mars Reconnaissance Orbiter. Also, the orbital settings for orbital settings for our simulations correspond to Mars Year (MY) 34 so that the time of the observations discussed in this paper corresponds to exactly the same conditions in the model.

The simulations are designed to examine the sensitivity and response of the distribution of water vapor to the GDS. We do not address the mechanism for the transport of dust to high altitudes or the formation of detached dust layers. Figure 1 shows the average model dust extinction profiles at the equator for the period during the strongest part of the storm ($L_s = 196\text{--}202^\circ$) compared with MCS measurements (v5.2.9). The dust optical extinction coefficients measured by MCS at a wavelength of $21.6 \mu\text{m}$ were scaled to visible wavelengths using a factor of 7.1 (Kleinböhl et al., 2011). For the non-GDS case, we use the dust horizontal and vertical distribution as it is calculated in the dust-lifting parameterization with efficiency parameters set for an average non-GDS year (Daerden et al., 2019; Neary & Daerden, 2018) and do not scale it to any climatology. In the GDS case with free dust (GDSfree), the same model settings are applied, but the total column dust optical depth is scaled on a daily basis to match the climatology of MY34 (Montabone et al., 2020). The GCM dust profile matches well with the MCS nighttime profile, but at heights above 40 km, the dust optical extinction coefficient profile remains below that of the MCS daytime profile (Figure 1). This may indicate that there are missing processes in the GCM that relate to daytime activity, for example subgrid-scale deep convective events that are currently not represented in the model (Daerden et al., 2015; Heavens et al., 2018; Spiga et al., 2013; Wang et al., 2018). To impose control over the vertical profile, we use a prescribed distribution based on Conrath (1975; also see Montmessin et al., 2004, for the equations). Using the typical value of the so-called Conrath parameter ($\nu=0.007$), the dust vertical profile decreases with altitude more rapidly than indicated by the observations from MCS at the time of the GDS (see simulation GDS007 in Figure 1), so we adapt the value of $\nu=0.0008$ to better match the observed profile of dust (simulation GDS0008, Figure 1).

The water cycle in GEM-Mars is described and evaluated against observational data sets in Neary and Daerden (2018), Smith et al. (2018), and Daerden et al. (2019). Water vapor and ice volume mixing ratios are stored as tracers that are transported by advection and eddy mixing. Water condenses into water ice when its partial pressure is above the saturation pressure (or the temperature drops below the frost point). For these simulations, we have made one modification relating to the ice particle size in the second half of the year. Previous simulations employed a cloud particle radius of 4 μm for radiative transfer calculations throughout the entire year, which led to good model-data comparisons for atmospheric temperatures and aphelion cloud belt (ACB) opacities during the aphelion season (Neary & Daerden, 2018). For the case of the 2018 GDS, (and nonaphelion season), smaller ice particle sizes are likely to apply (e.g., Clancy et al., 2010, 2019), and such particles lead to less dramatic cloud radiative feedbacks (Daerden et al., 2019). For the current simulations, we use ice particles with a radius of 2 μm in the second half of the year ($L_s > 180^\circ$).

3. Comparing Model Simulations and NOMAD Observations

The first water vapor profiles retrieved from NOMAD solar occultations in the IR were reported in Vandaele et al. (2019), but the full data set over the period of the 2018 GDS is presented in the accompanying paper of Aoki et al. (2019). There are 467 profiles available between $L_s = 180\text{--}240^\circ$. These profiles are by definition taken at the day-night terminator (morning or evening). The latitudes at which the profiles are measured are defined by the TGO orbit and vary through time across all latitudes (see Figure 2). The vertical profiles of tical profiles of water vapor were retrieved on an altitude grid with reference to the aeroid from 0 to 120 km with a vertical resolution of 1 km.

The GEM-Mars model output was interpolated to the exact latitude and longitude and to within 15-min local time of the NOMAD profiles. Because NOMAD takes a sunrise and a sunset solar occultation in each orbit, which is inclined at 74° , the NOMAD profiles are typically alternating between the northern and southern hemisphere on a daily basis. To make a concise plot that summarizes the NOMAD measurements in a meaningful way, the time series of the vertical profiles are split into northern and southern hemispheres (Figure 2). The current version of the NOMAD retrievals contains water vapor number densities. Approximate volume mixing ratios can be derived using model CO_2 number densities (Aoki et al., 2019); however during a GDS, the atmosphere will expand, and so the pressure scale height will change, and this will impact the actual CO_2 number densities. To compare model results only with directly retrieved quantities, we will consider the retrieved water vapor number densities here. As water densities span over several orders of magnitude in the vertical domain considered here (10–100 km), we present them on a logarithmic scale (Figure 2a). The latitude variation is overlaid on Figure 2 to indicate the spatial/temporal variability of the observations.

The collocated water vapor number density profiles from the different model simulations are plotted in the same way as the data in Figures 2b and 2c. The results from two simulations are compared: the MY34 simulations with Conrath parameter $\nu = 0.0008$ (GDS0008, Figure 2b) and the free dust simulation under non-GDS conditions (non-GDS, Figure 2c). The non-GDS simulation has much less water vapor than NOMAD, up to a factor $<1,000$ above 60 km, and by factors 10–100 between 20 and 40 km, particularly in the southern hemisphere (Figure 2c). In the GDS0008 simulation, water vapor densities are increasing above a height of 60 km and up to 80 km at the start of the GDS ($L_s \sim 195\text{--}200^\circ$), and the enhanced water vapor content extends up to heights of 100 km after $L_s \sim 210^\circ$. This corresponds well to the NOMAD observations in the GDS. During the onset of the GDS ($L_s \sim 195\text{--}200^\circ$), GDS0008 simulated water vapor densities remain below the NOMAD measurements above 80 km, but during the main phase of the GDS ($L_s \sim 210\text{--}230^\circ$), the match of the GDS0008 simulation with NOMAD is excellent.

4. Discussion

Properly simulating the dust profile between 40 and 80 km is crucial to improving the comparison between the observed and simulated water vapor density profiles. A Conrath parameter of $\nu = 0.0008$ provides a very good match with MCS dust profiles and also results in successful simulations of the water vertical profile at high altitude relative to NOMAD water vapor observations. It is expected that the precise shape of the dust profile will change over time, as the GDS evolves and declines. The value of the Conrath parameter applied

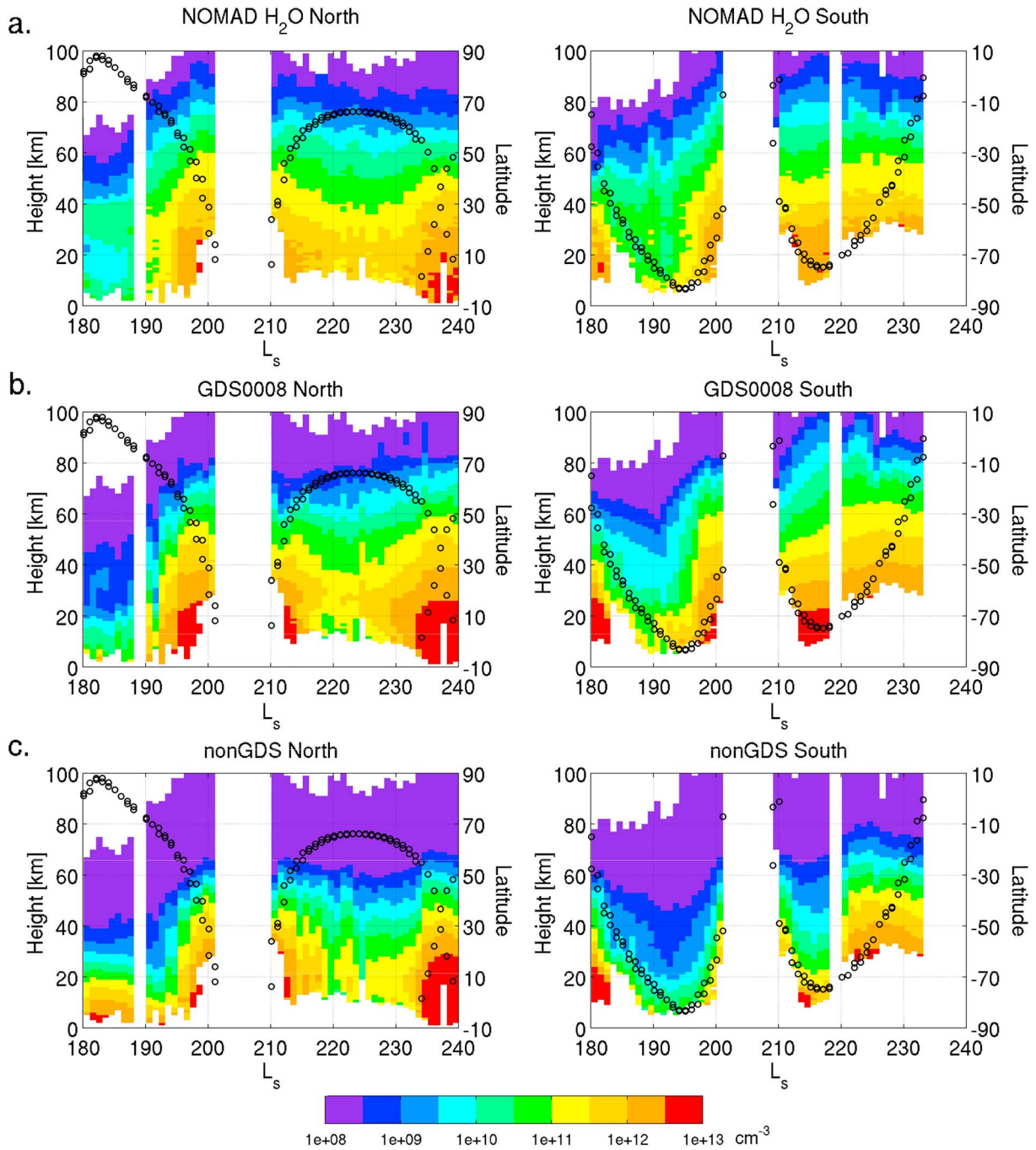


Figure 2. Water vapor number densities for northern (left) and southern (right) hemispheres for the period between L_s 180° and 240°, (a) as observed by Nadir and Occultation for Mars Discovery (NOMAD), (b) simulated by GEM-Mars using $\nu = 0.0008$, and (c) simulated by GEM-Mars for a non-global dust storm (GDS) case. The model results are at the same latitude (indicated by black circles, right axis), longitude, and L_s as the observations and within 15° local time of them. All profiles were averaged over 1° L_s bins.

in the GDS0008 simulation appears to be appropriate for the initial phase of the GDS as shown in Figure 1. At the start of the GDS, the layer of increased dust around 80 km seen in MCS data may cause additional heating and a further increase in high-altitude water vapor. This layer is difficult to implement using a simple Conrath description and was not considered in our simulations. In reality it may be caused by nonlocal deep convective events when the GDS develops (Heavens et al., 2018; Spiga et al., 2013; Wang et al., 2018).

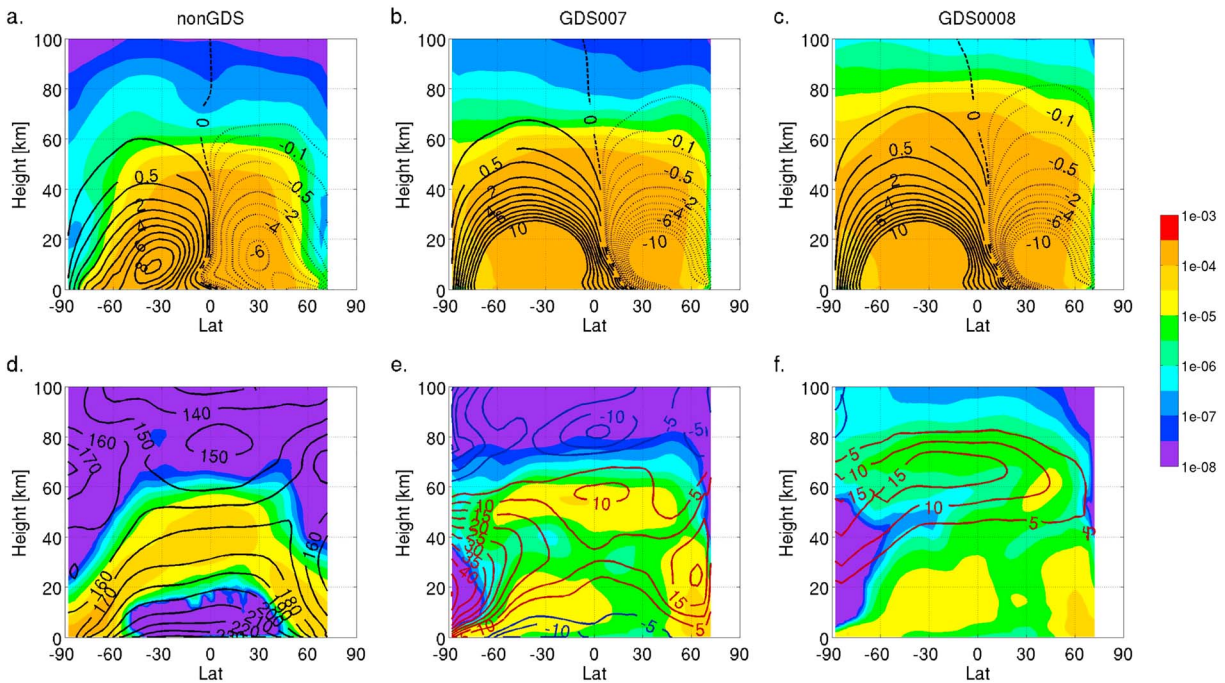


Figure 3. Daytime zonal mean profiles of water vapor (top row) and water ice (bottom row) volume mixing ratios (vmr, in ppmv) for the period of L_s 196–202° for three simulations, (a) non-GDS case, (b) Conrath $\nu = 0.007$ (GDS007), and (c) Conrath $\nu = 0.0008$ (GDS0008). Daytime meridional mass stream function contours ($\times 10^9$ kg/s) are shown in black in the top row. Full lines represent counterclockwise circulation, and dashed lines clockwise circulation. In the bottom row, contours are for temperature (in K) in the non-GDS case (d) and for the respective temperature differences GDS007-non-GDS (e) and GDS0008-GDS007 (f). Water ice vmr represents the number of water molecules in the ice phase relative to the total of air molecules. GDS = global dust storm.

During a GDS, two factors play a role in the increase of water vapor at high altitudes (40–100 km). One aspect is the enhanced global circulation, and the second is warmer temperatures in the 40- to 60-km range, which reduces the condensation of water vapor and the subsequent sedimentation of ice particles and allows the further transport of water vapor. The role and importance of these two mechanisms are illustrated in Figure 3, which shows zonal mean latitude-height cross sections of water vapor and ice water content averaged over the period $L_s=196\text{--}202^\circ$ for three different simulations. To examine the enhancement of the global circulation, contours of the daytime average meridional mass stream function are shown in Figures 3a–3c. For clarity, only daytime data are shown with solar zenith angles $< 80^\circ$. The non-GDS case (Figures 3a and 3d) represents the standard, nondust storm case where water vapor deposits on dust particles to form ice clouds at altitudes and latitudes where the water vapor partial pressure is equal to the saturation vapor pressure. The distribution of water and ice is very symmetric with latitude (owing to the season being near equinox). Due to the saturation and cloud formation at 30–50 km height, only small amounts of water continue to rise to higher altitudes as a result of the gravitational settling of the water ice particles. In the GDS007 simulation (Figures 3b and 3e) and the GDS0008 simulation (Figures 3c and 3f), which both have column optical depth scaled to the climatological values of MY34, two strong daytime Hadley circulation cells have developed due to the enhanced presence of dust in the lower atmosphere and its heating effect. The upwelling branches of the circulation cells transport dust upward and warm the equatorial atmosphere at heights up to 60 km (Figure 3e). There is a reduction in the water ice content around 40 km, but not enough to allow sufficient transport of water vapor above 60 km. The GDS0008 simulation (Figures 3c and 3f) only differs from the GDS007 one in the vertical distribution of dust above 40 km (see Figure 1). It results in a slightly enhanced circulation pattern above 40 km, but also in an additional strong increase in temperature (Figure 3f), preventing much more water vapor to condense and so less ice to sediment, so that water vapor can continue to rise to higher altitudes. This simulation results in water vapor mixing ratios at parts per million by volume level up to 100 km.

The GEM-Mars model includes gas-phase photochemistry (Daerden et al., 2019), which demonstrates how the increased water vapor over 40- to 100-km altitudes results in the production of H atoms in the upper

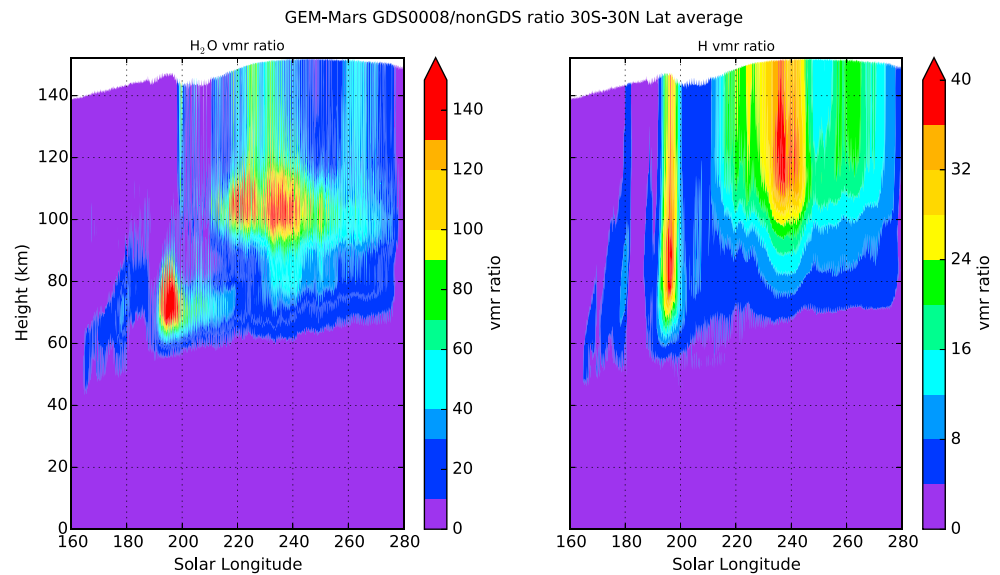


Figure 4. Ratio of simulated water vapor (left) and hydrogen (right) of two simulations, GDS0008/non-GDS (including atmospheric chemistry) in the equatorial region (between 30° N/S) for the period between $L_s=160\text{--}280^\circ$. GDS = global dust storm.

atmosphere. The model does not yet include specific routines for H escape, but a predicted increase in the abundance of H in the upper atmosphere can be linked to enhanced escape (see Chaffin et al., 2017, for a detailed discussion). In Figure 4, we show the ratio of the results from the GDS0008 and the non-GDS simulations for water vapor and hydrogen volume mixing ratios in the equatorial region between 30°S and 30°N. The onset of the GDS is very rapid around $L_s \sim 190^\circ$, and the water vapor profile responds with a large increase by more than a factor of 150 at a height of around 70 km. At this altitude, the photolysis of water vapor is strong, and atomic hydrogen is produced (see also Daerden et al., 2019, their Table 1 and Figure 1 for rates and reactions). The reaction rate of the strongest photolysis reaction (J11 in Daerden et al., 2019) is $\sim 10^{-6} \text{ s}^{-1}$ at 80 km and $\sim 3 \times 10^{-6} \text{ s}^{-1}$ at 100 km, which corresponds to a lifetime of ~ 11.5 and 3.8 sols, respectively. This is also the typical delay found in the simulations between the enhancement in water vapor and the resulting production of hydrogen. This delay of several sols is consistent with new data from the MAVEN spacecraft (Chaffin et al., 2019). There is a second injection of water vapor toward the end of the main GDS around $L_s \sim 240^\circ$, which causes an increase of hydrogen by a factor 40. The response is again rapid, with H being transported above 120 km within a few sols. After $L_s \sim 280^\circ$ the mixing ratios return to values similar to the non-GDS case.

5. Conclusions

The NOMAD and ACS instruments on ExoMars TGO observed a strong increase of water vapor at high altitudes (40–100 km) during the 2018 GDS. We presented the first detailed simulations in a 3-D GCM that are constrained by day-to-day dust optical depth maps for the time of the GDS and compare them directly with the NOMAD water vapor retrievals. It was found that the simulation of enhanced high-altitude water abundances is very sensitive to the vertical distribution of the dust. When a dust vertical profile is prescribed in the model that matches the profile observed by MCS, the model simulates a water vapor vertical distribution similar to what is observed by NOMAD. The extra dust in the atmosphere reinforces the global circulation below 40 km, but this alone does not explain how water vapor can ascend to 70–100 km, as is seen in the observations. In non-GDS conditions, saturation and ice cloud formation simulated at heights of 30–50 km prevents the upward transport of water to higher altitudes at the same volume mixing ratio (vmr) found at lower altitudes, since the water that deposited on ice particles falls through the ascending atmosphere. As a result, there is a decrease in the water vapor vmr at this altitude range, which is usually called the “hygro-pause.” In the GDS, temperatures are warmer in the 40- to 60-km altitude range, and saturation occurs in the

simulations at much higher altitudes (70–100 km). Our simulations show the sensitivity of this process to the vertical profile of dust. If there is not enough dust above 40 km, the enhanced circulation below 40 km does not heat the hygro-pause sufficiently to prevent strong ice cloud formation. When the dust profile is set to match the profile observed by MCS, the heating is strong enough, and water can continue to rise at constant vmr to such altitudes, as is observed by NOMAD. At the greater temperatures in the GDS, there were fewer clouds, and there would be less water deposited on the ice particles.

Photodissociation of water vapor is most rapid at heights above 90 km, and our model predicts that the enhanced water vapor abundances at these altitudes during the 2018 GDS cause an increase in H atoms by almost 2 orders of magnitude. The response of H above 120 km to the H₂O increase is typically a few sols. This result supports the hypothesis that dust storms can enhance atmospheric loss through H escape (Chaffin et al., 2017; Heavens et al., 2018).

Acknowledgments

This work was made possible thanks to the reconstructed gridded and kriged maps of column dust optical depth from Mars Climate Sounder observations provided by L. Montabone. The dust maps were prepared using MCS v5.3 thanks to A. Kleinböhl and D. Kass. Dust climatologies can be found at the following link: (http://www-mars.lmd.jussieu.fr/mars/dust_climatology/). The MCS v5.29 data are available from the NASA Planetary Data System (PDS) at the following link: (https://pds-atmospheres.nmsu.edu/data_and_services/atmospheres_data/Mars/Mars.html). The results from the GEM-Mars GCM simulations used in this article are available on the BIRA-IASB data repository (<http://repository.aeronomie.be>). ExoMars is a space mission of the European Space Agency (ESA) and Roscosmos. The NOMAD experiment is led by the Royal Belgian Institute for Space Aeronomy (IASB-BIRA), assisted by Co-PI teams from Spain (IAA-CSIC), Italy (INAF-IAPS), and the United Kingdom (Open University). This project acknowledges funding by the Belgian Science Policy Office (BELSPO), with the financial and contractual coordination by the ESA Prodex Office (PEA 4000103401 and 4000121493); by U.K. Space Agency through Grant ST/R005761/1; and by Italian Space Agency through Grant 2018-2-HH.0. This work was supported by the Belgian Fonds de la Recherche Scientifique – FNRS under Grants 30442502 (ET_HOME) and T.0171.16 (CRAMIC) and BELSPO BrainBe SCOOP Project. U.S. investigators were supported by the National Aeronautics and Space Administration. Canadian investigators were supported by the Canadian Space Agency.

References

- Aoki, S., Vandaele, A. C., Daerden, F., Villanueva, G. L., Liuzzi, G., Thomas, I. R., et al. (2019). Water vapor vertical profile on Mars in dust storms observed by TGO/NOMAD *Journal of Geophysical Research: Planets*, *124*, 3482–3497. <https://doi.org/10.1029/2019JE006109>
- Bohren, C. F., & Huffman, D. R. (1983). *Absorption and scattering of light by small particles*. New York: Wiley.
- Chaffin, M. S., Deighan, J., Schneider, N. M., & Stewart, A. I. F. (2017). Elevated atmospheric escape of atomic hydrogen from Mars induced by high-altitude water. *Nature Geoscience*, *10*(3), 174–178. <https://doi.org/10.1038/ngeo2887>
- Chaffin, M. S., D. M. Kass, S. Aoki, A. A. Fedorova, J. Deighan, J.-Y. Chaufray, et al. (2019). Mars climate controls atmospheric escape: Dust-driven escape from surface to space with MRO/MCS, TGO/NOMAD, TGO/ACS, and MAVEN/IUVS, The Ninth International Conference on Mars abstract, submitted.
- Clancy, R. T., Wolff, M. J., Smith, M. D., Kleinböhl, A., Cantor, B. A., Murchie, S. L., et al. (2019). The distribution, composition, and particle properties of Mars mesospheric aerosols: An analysis of CRISM visible/near-IR limb spectra with context from near-coincident MCS and MARCI observations. *Icarus*, *328*, 246–273. <https://doi.org/10.1016/j.icarus.2019.03.025>
- Clancy, R. T., Wolff, M. J., Whitney, B. A., Cantor, B. A., Smith, M. D., & McConnochie, T. H. (2010). Extension of atmospheric dust loading to high altitudes during the 2001 Mars dust storm: MGS TES limb observations. *Icarus*, *207*(1), 98–109. <https://doi.org/10.1016/j.icarus.2009.10.011>
- Conrath, B. J. (1975). Thermal structure of the Martian atmosphere during the dissipation of the dust storm of 1971. *Icarus*, *24*(1), 36–46. [https://doi.org/10.1016/0019-1035\(75\)90156-6](https://doi.org/10.1016/0019-1035(75)90156-6)
- Daerden, F., Neary, L., Viscardi, S., Garcia Muñoz, A., Clancy, R. T., Smith, M. D., et al. (2019). Mars atmospheric chemistry simulations with the GEM-Mars general circulation model. *Icarus*, *326*, 197–224. <https://doi.org/10.1016/j.icarus.2019.02.030>
- Daerden, F., Whiteway, J. A., Neary, L., Komguem, L., Lemmon, M. T., Heavens, N. G., et al. (2015). A solar escalator on Mars: Self-lifting of dust layers by radiative heating. *Geophysical Research Letters*, *42*, 7319–7326. <https://doi.org/10.1002/2015GL064892>
- Encrenaz, T., Greathouse, T. K., Aoki, S., Daerden, F., Giuranna, M., Forget, F., et al. (2019). Ground-based infrared mapping of H₂O₂ on Mars near opposition. *Astronomy & Astrophysics*, *627*, A60. <https://doi.org/10.1051/0004-6361/201935300>
- Fedorova, A., Bertaux, J.-L., Betsis, D., Montmessin, F., Korabiev, O., Maltagliati, L., & Clarke, J. (2018). Water vapor in the middle atmosphere of Mars during the 2007 global dust storm. *Icarus*, *300*, 440–457. <https://doi.org/10.1016/j.icarus.2017.09.025>
- Giuranna, M., Viscardi, S., Daerden, F., Neary, L., Etiopie, G., Oehler, D., et al. (2019). Independent confirmation of a methane spike on Mars and a source region east of Gale Crater. *Nature Geoscience*, *12*(5), 326–332. <https://doi.org/10.1038/s41561-019-0331-9>
- Heavens, N. G., Kleinböhl, A., Chaffin, M. S., Halekas, J. S., Kass, D. M., Hayne, P. O., et al. (2018). Hydrogen escape from Mars enhanced by deep convection in dust storms. *Nature Astronomy*, *2*(2), 126–132. <https://doi.org/10.1038/s41550-017-0353-4>
- Holton, J. R., & Gettelman, A. (2001). Horizontal transport and the dehydration of the stratosphere. *Geophysical Research Letters*, *28*(14), 2799–2802. <https://doi.org/10.1029/2001GL013148>
- Kleinböhl, A., Schofield, J. T., Abdou, W. A., Irwin, P. G. J., & de Kok, R. J. (2011). A single-scattering approximation for infrared radiative transfer in limb geometry in the Martian atmosphere. *Journal of Quantitative Spectroscopy and Radiative Transfer*, *112*, 1568–1580. <https://doi.org/10.1016/j.jqsrt.2011.03.006>
- Kleinböhl, A., Schofield, J. T., Kass, D. M., Abdou, W. A., Backus, C. R., Sen, B., et al. (2009). Mars Climate Sounder limb profile retrieval of atmospheric temperature, pressure, and dust and water ice opacity. *Journal of Geophysical Research*, *114*, E100006. <https://doi.org/10.1029/2009JE003358>
- Korabiev, O., Montmessin, F., Trokhimovskiy, A., Fedorova, A. A., Shakun, A. V., Grigoriev, A. V., et al. (2018). The Atmospheric Chemistry Suite (ACS) of three spectrometers for the ExoMars 2016 Trace Gas Orbiter. *Space Science Reviews*, *214*, 7. <https://doi.org/10.1007/s11214-017-0437-6>
- Korabiev, O., Vandaele, A. C., Montmessin, F., Fedorova, A. A., Trokhimovskiy, A., Forget, F., et al., & The ACS and NOMAD Science Teams (2019). No detection of methane on Mars from early ExoMars Trace Gas Orbiter observations. *Nature*, *568*, 517–520. <https://doi.org/10.1038/s41586-019-1096-4>
- Krasnopolsky, V. A. (2019). Photochemistry of water in the Martian thermosphere and its effect on hydrogen escape. *Icarus*, *321*, 62–70. <https://doi.org/10.1016/j.icarus.2018.10.033>
- Madeleine, J.-B., Forget, F., Millour, E., Montabone, L., & Wolff, M. J. (2011). Revisiting the radiative impact of dust on Mars using the LMD Global Climate Model. *Journal of Geophysical Research*, *116*(E11), E11010. <https://doi.org/10.1029/2011JE003855>
- Montabone, L., Forget, F., Millour, E., Wilson, R. J., Lewis, S. R., Cantor, B., et al. (2015). Eight-year climatology of dust optical depth on Mars. *Icarus*, *251*, 65–95. <https://doi.org/10.1016/j.icarus.2014.12.034>
- Montabone, L., Spiga, A., Kass, D. M., Kleinböhl, A., Forget, F., & Millour, E. (2020). Martian Year 34 column dust climatology from Mars climate sounder observations: Reconstructed maps and model simulations. *Journal of Geophysical Research: Planets*, *125*, e2019JE006111. <https://doi.org/10.1029/2019JE006111>

- Montmessin, F., Forget, F., Rannou, P., Cabane, M., & Haberle, R. M. (2004). Origin and role of water ice clouds in the Martian water cycle as inferred from a general circulation model. *Journal of Geophysical Research, Planets*, 1991–2012, 109. <https://doi.org/10.1029/2004je002284>
- Musioli, G., Kruss, M., Demirci, T., Schräski, B., Teiser, J., Daerden, F., et al. (2018). Saltation under Martian gravity and its influence on the global dust distribution. *Icarus*, 306, 25–31. <https://doi.org/10.1016/j.icarus.2018.01.007>
- Neary, L., & Daerden, F. (2018). The GEM-Mars general circulation model for Mars: Description and evaluation. *Icarus*, 300, 458–476. <https://doi.org/10.1016/j.icarus.2017.09.028>
- Shaposhnikov, D. S., Medvedev, A. S., Rodin, A. V., & Hartogh, P. (2019). Seasonal water “pump” in the atmosphere of Mars: Vertical transport to the thermosphere. *Geophysical Research Letters*, 46, 4161–4169. <https://doi.org/10.1029/2019GL082839>
- Smith, M., Daerden, F., Neary, L., & Khayat, S. (2018). The climatology of carbon monoxide and water vapor on Mars as observed by CRISM and modeled by the GEM-Mars general circulation model. *Icarus*, 301, 117–131. <https://doi.org/10.1016/j.icarus.2017.09.027>
- Spiga, A., Faure, J., Madeleine, J.-B., Määttä, A., & Forget, F. (2013). Rocket dust storms and detached dust layers in the Martian atmosphere. *Journal of Geophysical Research: Planets*, 118, 746–767. <https://doi.org/10.1002/jgre.20046>
- Toon, O. B., McKay, C. P., & Ackerman, T. P. (1989). Rapid calculation of radiative heating rates and photodissociation rates in inhomogeneous multiple scattering atmospheres. *Journal of Geophysical Research*, 94(D13), 16,287–16,301. <https://doi.org/10.1029/JD094iD13p16287>
- Vandaele, A. C., Korabely, O., Daerden, F., Aoki, S., Thomas, I. R., Altieri, F., et al., & NOMAD Science Team, and ACS Science Team (2019). Martian dust storm impact on atmospheric H₂O and D/H observed by ExoMars Trace Gas Orbiter. *Nature*, 568, 521–525. <https://doi.org/10.1038/s41586-019-1097-3>
- Vandaele, A. C., Lopez-Moreno, J.-J., Patel, M. R., Bellucci, G., Allen, M., Alonso-Rodrigo, G., et al., & and the NOMAD Team (2018). NOMAD, an integrated suite of three spectrometers for the ExoMars Trace Gas mission: Technical description, science objectives and expected performance. *Space Science Reviews*, 214, 80. <https://doi.org/10.1007/s11214-018-0517-2>
- Wang, C., Forget, F., Bertrand, T., Spiga, A., Millour, E., & Navarro, T. (2018). Parameterization of rocket dust storms on Mars in the LMD Martian GCM: Modeling details and validation. *Journal of Geophysical Research: Planets*, 123(4), 982–1000. <https://doi.org/10.1002/2017JE005255>
- Warren, S. G., & Brandt, R. E. (2008). Optical constants of ice from the ultraviolet to the microwave: A revised compilation. *Journal of Geophysical Research*, 113(D14), D14220. <https://doi.org/10.1029/2007JD009744>